Materials & Design 254 (2025) 114043

Contents lists available at ScienceDirect

Materials & Design

journal homepage: www.elsevier.com/locate/matdes

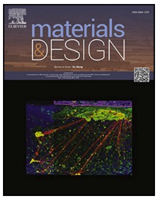

Melt pool dynamics and pore formation in selective laser melting: Mechanisms and microstructural insights[☆]

Jiafei Pang [a], Liming Huang [a], Hailin Liu [a], Xin Yi [a,b,*]

[a] School of Mechanics and Engineering Science, Peking University, Beijing 100871, China
[b] HEDPS, Center for Applied Physics and Technology, Peking University, Beijing 100871, China

ARTICLE INFO

Editor: Xu Song

Keywords:
Additive manufacturing
CFD simulations
Ray reflection
Pore defects
Microstructure

ABSTRACT

Selective laser melting (SLM) is an advanced additive manufacturing technique, yet its application for structural components is often constrained by porosity-related defects. This study elucidates keyhole collapse and pore formation mechanisms through single-track simulations, combining ray-tracing-based heat source modeling and computational fluid dynamics (CFD) to analyze melt pool dynamics. Depending on the ratio of laser power density to scanning speed, two distinct melt pool behaviors are analyzed: keyhole mode and conduction mode. In the keyhole mode, protrusions on the front and rear keyhole walls, driven by recoil pressure and reflected laser rays, merge to trap gas, causing truncation and pore formation. Alternatively, backfilling, driven by surface tension during excessive keyhole curvature, allows gas escape and avoids pore defect formation. In the conduction mode, smaller protrusions and stable melt pool behavior without collapse are observed, with melt pool depth fluctuations attributed to nonuniform powder distribution. Coupling CFD with a cellular automaton model highlights the dual impact of pores on material microstructure: grain growth obstruction leads to coarser grains above pores, while reduced thermal gradients near pores promote fine grain formation. These findings deepen understanding of pore formation and its microstructural effects, providing insights to optimize SLM processes for enhanced material performance.

1. Introduction

SLM is a widely used additive manufacturing technique that has garnered significant attention in aerospace, transportation, and biomedical engineering. By selectively melting and fusing metal powders layer by layer, SLM enables the fabrication of high-precision metal components with complex geometries. This process offers speed and cost advantages over traditional manufacturing methods, such as casting, machining, and forging [1]. However, SLM-fabricated components are often plagued by defects, including pores, cracks, and excessive surface roughness, which limit their structural integrity and performance [2–7]. While post-processing techniques, such as heat treatment and polishing, can enhance product quality, these methods are labor-intensive, expensive, and less effective for intricate geometries. To minimize pore defects, it is crucial to develop a thorough understanding of melt pool dynamics, pore formation mechanisms, and their influence on microstructure evolution during the scanning process.

Reducing defects in SLM components remains challenging due to the complex interactions and competing technical demands involved. While higher laser power density mitigates balling and ensures complete melting, it also promotes keyhole formation, increasing the likelihood of pore defects within deep, narrow cavities [8,9]. These pores, as experiments have shown, often concentrate at the bottom of keyholes, where trapped gas exacerbates defect formation [10–12]. While experimental approaches, such as varying scanning speed and powder thickness, can shed light on print quality [5,13], they are costly and fail to capture the real-time dynamics of melt pool evolution. This limitation underscores the critical role of numerical simulations in elucidating melt pool behavior and mitigating defect formation.

Numerical simulations have emerged as powerful tools for investigating defect formation mechanisms in SLM. The CFD is widely used to model melt pool dynamics [14], while phase-field and cellular automaton (CA) models simulate heat transfer, melting, and microstructure evolution [15,16]. These methods have been particularly effective in studying pore-related phenomena [4,8,17–19]. For instance, Tan et al. examined how environmental pressure influences pore size [17], and

---

[☆] This article is part of a special issue entitled: 'Additive Manufacturing' published in Materials & Design.

[*] Corresponding author.
E-mail address: xyi@pku.edu.cn (X. Yi).

https://doi.org/10.1016/j.matdes.2025.114043
Received 18 July 2024; Received in revised form 16 April 2025; Accepted 2 May 2025

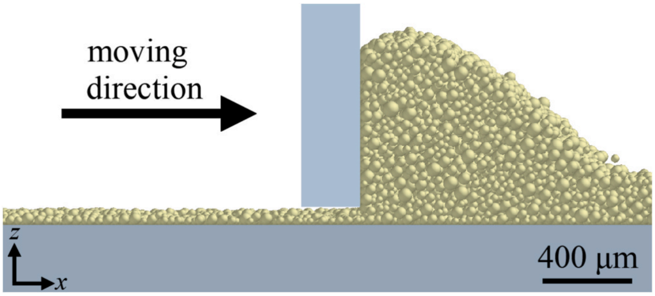

Fig. 1. Schematic diagram of the powder coating simulation process.

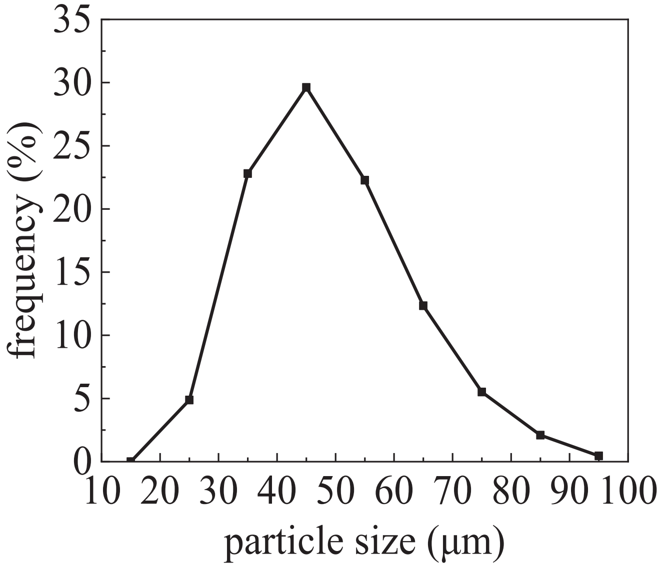

Fig. 2. Simulated particle size distribution of the 316L stainless steel powder, generated based on our experimental measurements.

Tang et al. demonstrated the contribution of high energy density to pore defects [19]. Additionally, ray tracing is employed to reveal how surface tension collapses keyhole walls, causing pore formation [4], while other studies have highlighted the roles of unsteady molten flow [18] and incomplete particle melting [4].

Despite these advancements, critical gaps remain in understanding the influence of laser-ray reflection and its interactions with the keyhole on defect formation. In this study, we simulate single-track scanning under varying laser power and scanning speed conditions. By integrating a ray-tracing heat source with the finite volume method (FVM), we investigate how laser interacts with the melt pool, and elucidate keyhole collapse and pore formation mechanisms. Two melt pool behaviors are comprehensively analyzed: keyhole mode and conduction mode, highlighting the roles of recoil pressure, reflected laser rays, and surface tension in regulating melt pool evolution and pore formation. Moreover, the impact of pores on material microstructure is explored. Coupling CFD with a CA model, we analyze the dual influence of pores on grain growth: obstructing grains leads to coarser grains above pores, while reduced thermal gradients near pores encourage fine grain formation. These results provide critical insights into the interplay of melt pool dynamics, defect formation, and microstructure evolution, offering pathways for optimizing SLM processes to enhance material performance.

2. Simulation models

The SLM process comprises various intricate stages, including powder spreading, melting of the powder bed, and microstructure evolution. Each stage requires distinct methodologies for accurate simulation. The discrete element method (DEM) was employed to simulate the powder spreading process and obtain the initial configuration of the powder bed. The FVM simulations were conducted to model the melting of the powder bed and the subsequent evolution of the melt pool. The CA model was utilized to analyze the microstructure of the material following solidification. The following subsections 2.1–2.5 briefly describe the details of these simulation models.

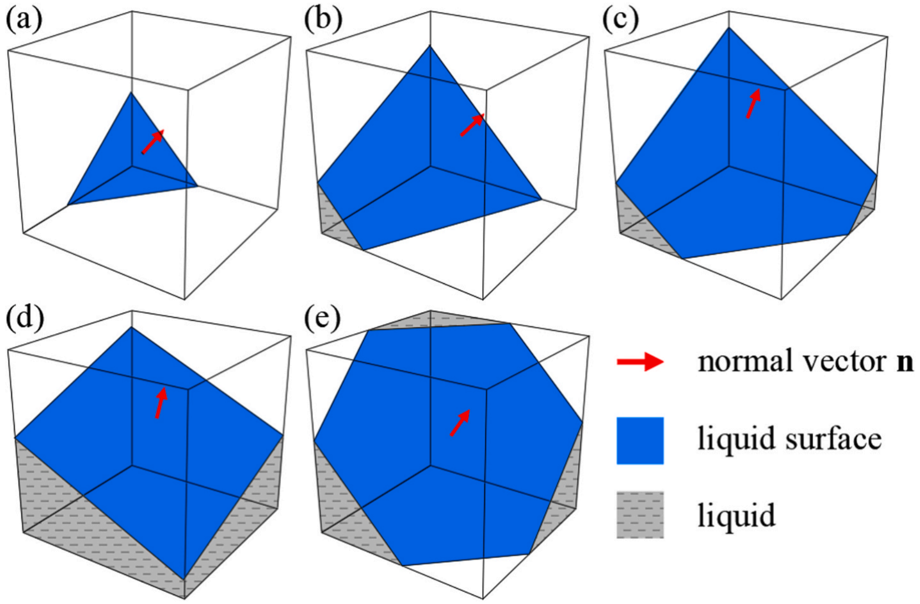

Fig. 3. Five representative configurations of the fluid surface in the PLIC scheme for $0 < f < 0.5$. Panels (a)–(d) illustrate cases where one, two, three, or four coplanar vertices lie beneath the fluid surface (blue planes) within a cell. Panel (e) depicts a scenario with four non-coplanar vertices beneath the fluid surface. For $0.5 < f < 1$, the transformed parameters $f' = 1 - f$, $\mathbf{n}' = -\mathbf{n}$, and $\mathbf{x}' = 1 - \mathbf{x}$ are used to determine the fluid surface position following the same method as for $0 < f < 0.5$.

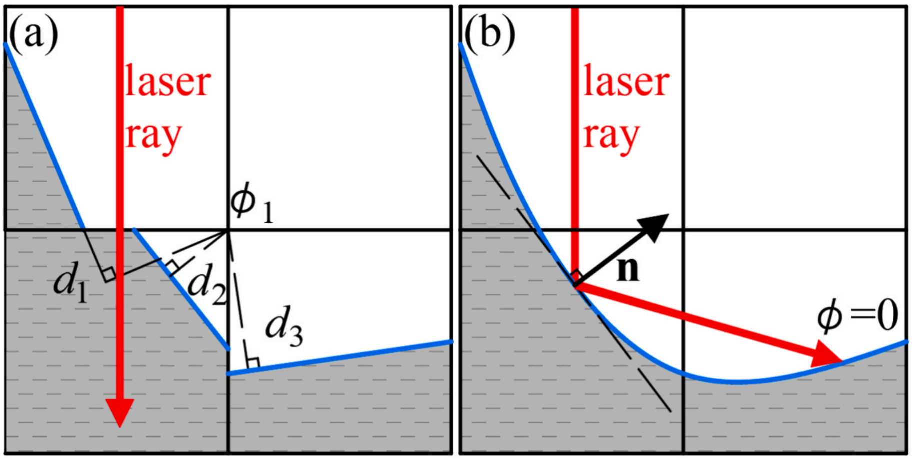

Fig. 4. (a) Illustration of a laser ray unphysically penetrating the fluid through a gap between discontinuous fluid planes (blue lines) constructed using the PLIC scheme. (b) Representation of a laser ray being physically reflected by the reconstructed continuous fluid surface (refraction not depicted).

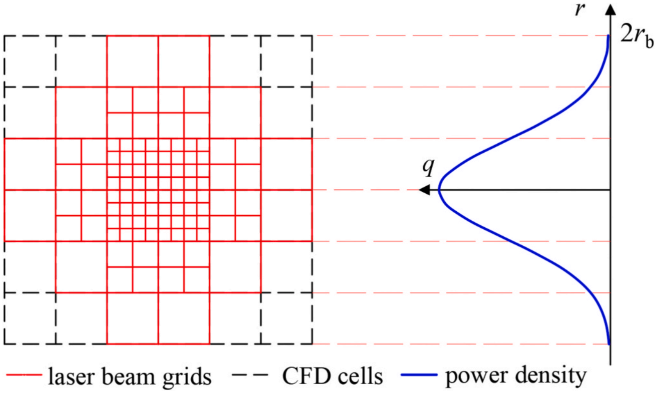

Fig. 5. Schematics of power density distribution and discretization of the laser beam.

2.1. Powder bed model

The powder bed serves as the foundation for melt pool simulations, and its initial configuration was constructed using DEM. Fig. 1 illustrates the formation process of a high-density powder bed. Mimicking the actual powder deposition process, the powder is first deposited onto the substrate and then leveled to a specified thickness using a coating plate [20]. The size distribution of the 316L stainless steel powder is presented in Fig. 2. The resulting DEM data, containing detailed information on particle positions and radii, is used to generate an STL file that accurately represents the powder bed structure.

2.2. Reconstruction of the fluid surface

In the CFD simulations, a cell is identified as a surface cell when the volume fraction f of the fluid (including metal below the solidus temperature, treated as solidified fluid) within the cell lies between 0 and 1. Accurate determination of the laser-fluid surface intersection and laser reflection requires constructing the fluid surface. This is achieved using the piecewise linear interface calculation (PLIC) scheme [21] combined with the volume of fluid (VOF) method [22]. In the PLIC scheme, the free fluid surface is represented by piecewise planar segments across different cells. Representative configurations of the fluid surface in the PLIC scheme are shown in Fig. 3. These planar segments are positioned based on the volume fraction f and the surface unit normal vector $\mathbf{n}$, calculated as $\mathbf{n} = -\nabla f / |\nabla f|$, where ∇ denotes the gradient operator.

Since the PLIC scheme does not ensure continuity between adjacent surface cells, potentially causing gaps between fluid planes (Fig. 4a). These discontinuities can result in unphysical laser penetration through the fluid instead of proper absorption and reflection. To address this, the discontinuous surface planes constructed by the PLIC method are adjusted using a trilinear interpolation method [23], creating a continuous, though not necessarily smooth, fluid surface (Fig. 4b). This reconstruction ensures accurate modeling of the fluid surface, minimizing errors in laser interaction. The continuous surface allows precise determination of the laser-fluid intersection point and the associated surface normal vector $\mathbf{n}$.

The reconstruction of a continuous fluid surface using the trilinear interpolation method is summarized as follows. For a given vertex i, surrounded by N fluid surface planes constructed via the PLIC method, the average distance ϕ_i between vertex i and these N fluid planes is calculated as $\phi_i = \sum_{j=1}^{N} d_j / N$, where d_j is the directed distance from vertex i to the j-th fluid plane. The sign of d_j is positive if vertex i is above the j-th fluid plane and negative if below. A parallelepiped surface cell has eight vertices, and its reconstructed surface patch is determined using a trilinear interpolation scheme over these eight vertices, given by

$$\phi(x, y, z) = \sum_{i=1}^{8} \phi_i \left(1 - \frac{|x - x_i|}{\Delta x_c}\right) \left(1 - \frac{|y - y_i|}{\Delta y_c}\right) \left(1 - \frac{|z - z_i|}{\Delta z_c}\right) = 0$$

where Δx_c, Δy_c, and Δz_c are the dimensions of the surface cell, and x_i, y_i, and z_i are the Cartesian coordinates of vertex i (=1,2,..,8). Applying this scheme to all surface cells ensures a continuous fluid surface. The intersection of a laser ray with the fluid surface is identified by solving the equation $\phi(x,y,z) = 0$ in combination with the laser ray equation. At the intersection, the unit normal vector $\mathbf{n}$ of the fluid surface is computed as $\mathbf{n} = \nabla \phi / |\nabla \phi|$, which is then used for calculating the laser reflection.

2.3. Generation of rays

In our simulations, the laser beam is discretized into a set of rays according to its power density distribution. The interaction between the laser beam and the fluid surface—encompassing reflection and energy absorption—is modeled by tracing the intersection points of these rays with the reconstructed fluid surface.

Assuming a near-Gaussian distribution, the power density q of the laser beam is given by

$$q = \frac{2P_l}{\pi r_b^2} \exp\left(-\frac{2r^2}{r_b^2}\right)$$

where P_l is the total power of the laser beam, r_b is the laser spot radius, and r is the radial distance from the beam center. Approximately 99.6 % of the total laser energy is contained within $r < 2r_b$, so the energy beyond this region is neglected.

Fig. 5 illustrates the discretization of the laser beam based on its energy density. To prevent excessive energy concentration in individual rays, the laser beam grid is densified near the beam center, where energy density is highest, and coarsened farther out to improve computational efficiency. Each red block in Fig. 5 represents a ray centered within it. The lateral dimensions of each CFD cells are equally divided into N_r segments, resulting in N_r^2 laser beam grids. As the power distribution of the laser is non-uniform, the value of N_r depends on the value of the local power density q. The power P_r of each ray satisfies

$$P_r = q(x,y)\frac{\Delta x_c \Delta y_c}{N_r^2(x,y)} < P_{r,\max}$$

where Δx_c and Δy_c are the lateral sizes of the CFD cells, and $P_{r,\max}$ is the maximum allowable energy for each ray. In our simulations, $P_{r,\max} = 2P_l \Delta x_c \Delta y_c / (25\pi r_b^2)$ is taken, and N_r is chosen as the smallest integer satisfying the above inequality.

The effective reflectivity or reflection coefficient, defined as the ratio of reflected power to incident power, is calculated using the Fresnel equation as [24]

$$R_{\text{eff}} = \frac{1}{2}\left|\frac{\hat{n}^2\cos\theta_i - (\hat{n}^2 - \sin^2\theta_i)^{1/2}}{\hat{n}^2\cos\theta_i + (\hat{n}^2 - \sin^2\theta_i)^{1/2}}\right|^2 + \frac{1}{2}\left|\frac{\cos\theta_i - (\hat{n}^2 - \sin^2\theta_i)^{1/2}}{\cos\theta_i + (\hat{n}^2 - \sin^2\theta_i)^{1/2}}\right|^2 \quad (1)$$

where $\hat{n}$ is the complex refractive index of the metallic material, and θ_i is the angle of incidence. For each reflection, the power P_t of a transmitted laser ray is

$$P_t = (1 - R_{\text{eff}})P_i$$

where P_i is the power of the incident ray. The reflected ray, with power $R_{\text{eff}}P_i$, may either serve as an incident ray in subsequent time steps or exit the computational domain. The direction $\mathbf{s}_r$ of the reflected ray is determined by [25].

$$\mathbf{s}_r = \mathbf{s}_i - 2\mathbf{n}(\mathbf{n}\cdot\mathbf{s}_i)$$

where $\mathbf{s}_i$ is the direction vector of the incident ray, and $\mathbf{n}$ is the normal vector of the fluid surface at the intersection point. With each reflection, the energy of the laser ray decreases. The reflection process continues until the remaining power of the laser ray falls below 5 % of its initial value.

In most cases, the penetration depth of the laser in metal is minimal, causing the transmitted energy to be fully absorbed by the first cell the laser enters. However, in certain extreme scenarios, such as when the intersection cell contains little or no liquid, the laser may penetrate further [26]. To account for this, we consider laser refraction and attenuation within the fluid and redistribute the absorbed energy based on the penetration distance. The direction of the refracted ray is determined by Snell's law. According to the laser attenuation function, the power $P_{a,i}$ of the laser energy from a single ray absorbed by the i-th cell is

$$P_{a,i}(l_i) = P_{t,i}(1 - e^{-\alpha l_i})$$

where $\alpha = 4\pi k/\lambda$ is the absorption coefficient, k is the imaginary part of the refractive index $\hat{n}$, λ is the wavelength, $P_{t,i}$ is the power of the laser entering the i-th cell, and l_i is the penetration distance within the i-th cell. For the first cell through which the laser passes, $P_{t,1} = P_t$; for subsequent cells, $P_{t,i} = P_{t,i-1} - P_{a,i-1}$. The calculation of the transmitted laser energy ends when $P_{t,i}$ falls below 5 % of the initial transmitted power P_t.

2.4. The CFD model

The CFD simulations, incorporating classical fluid mechanics, recoil pressure, and heat and mass transfer, are essential for simulating melt pool evolution in SLM. The melt pool flow is assumed to be incompressible, laminar, and Newtonian, governed by the conservation equations for mass, momentum, and energy as

$$\frac{\partial\rho}{\partial t} + \nabla\cdot(\rho\mathbf{v}) = 0,$$

$$\frac{\partial(\rho\mathbf{v})}{\partial t} + \nabla\cdot(\rho\mathbf{v}\otimes\mathbf{v}) = -\nabla p + \nabla\cdot(\mu\nabla\mathbf{v}) + \mathbf{F},$$

$$\frac{\partial(\rho h)}{\partial t} + \nabla\cdot(\rho h\mathbf{v}) = \nabla\cdot(\kappa\nabla T) + \dot{Q}.$$

Here, t is time, ρ is fluid density, $\mathbf{v}$ is velocity, μ is viscosity, p is pressure, $\mathbf{F}$ is the body force per unit volume (primarily including contributions from recoil pressure, surface tension, and Marangoni force, though other forces such as gravity are also considered but are less significant in comparison), h is specific enthalpy, κ is thermal conductivity, T is temperature, and $\dot{Q}$ is the thermal flux term.

Note that many material properties, such as density ρ, viscosity μ, and surface tension γ, are temperature-dependent and vary with the state of matter. Below the solidus temperature T_s or above the liquidus temperature T_l, these parameters take values corresponding to the solid or liquid states, respectively. Between T_s and T_l, the parameter values in simulations are interpolated linearly [27]. For example, fluid density ρ at $T_s < T < T_l$ is given by

$$\rho = \frac{T - T_s}{T_l - T_s}\rho_s + \frac{T_l - T}{T_l - T_s}\rho_l$$

where ρ_s and ρ_l are the densities of the solid and liquid phases, respectively. Other temperature-dependent parameters are interpolated using the same approach.

During SLM, laser irradiation raises the melt pool temperature above the boiling point, leading to rapid evaporation and generating recoil pressure. This recoil pressure induces a concave deformation in the melt pool. Using the Clausius-Clapeyron equation, the recoil pressure p_r is given by [26]

$$p_r = 0.54p_0\exp\left[\frac{L_v M}{R_g}\left(\frac{1}{T_v} - \frac{1}{T}\right)\right] \quad (2)$$

where p_0 is ambient pressure (1.01×10^5 Pa), L_v is the latent heat of evaporation, R_g is the gas constant, M is the molar mass, and T_v is the evaporation (boiling) temperature. The recoil pressure p_r is then converted into an equivalent body force $\mathbf{F}_r$ as

$$\mathbf{F}_r = -|\nabla f|p_r\mathbf{n}$$

where the term $|\nabla f|$ transforms an surface force per unit area into a volumetric surface force [28].

At the microscale, surface tension is a critical factor influencing melt pool morphology and stability. The surface tension γ contributes to the body force $\mathbf{F}_s$ (or a volumetric surface force) in the momentum equation as [28]

$$p_c = -\gamma(\nabla\cdot\mathbf{n})\mathbf{F}_s = |\nabla f|p_c\mathbf{n} \quad (3)$$

where p_c is the capillary pressure associated with the surface tension.

The temperature gradient of surface tension induces the Marangoni force $\mathbf{F}_M$, which drives fluid motion and contributes to the body force as [28]

$$\mathbf{F}_M = \frac{d\gamma}{dT}[\nabla T - (\mathbf{n}\cdot\nabla T)\mathbf{n}]|\nabla f| \quad (4)$$

For 316L stainless steel, the surface tension γ decreases with increasing

Table 1

Material properties of 316L stainless steel [12].

Parameters	Values
Density of solid ρ_s (kg m^{-3})	7900
Density of liquid ρ_l (kg m^{-3})	$7433 + 0.0393T - 1.8 \times 10^{-4}T^2$
Specific heat of solid (J kg^{-1} K^{-1})	$462 + 0.134T$
Specific heat of liquid (J kg^{-1} K^{-1})	775
Thermal conductivity κ of solid (W m^{-1} K^{-1})	$9.248 + 0.01571T$
Thermal conductivity κ of liquid (W m^{-1} K^{-1})	$12.41 + 0.003279T$
Evaporation temperature T_v (K)	3090
Solidus temperature T_s (K)	1658
Liquidus temperature T_l (K)	1723
Molar mass M (kg mol^{-1})	0.05593
Viscosity μ (kg m^{-1} s^{-1})	0.006
Surface tension γ (N m^{-1})	$1.943 - 0.00043(T - T_s)$
Latent heat of fusion L_s (J kg^{-1})	2.7×10^5
Latent heat of evaporation L_v (J kg^{-1})	7.45×10^6
Emissivity ε	0.4
Heat transfer coefficient h (kg s^{-3} K^{-1})	80
Refractive index $\hat{n}$	3.27 + 4.48 i

T is temperature in Kelvin (K).

temperature.

The recoil pressure given in Eq. (2) and the capillary pressure in Eq. (3) act normal to the melt pool surface, while the Marangoni force in Eq. (4) acts tangentially. These aspects drive melt pool dynamics, and their influence on keyhole stability is analyzed in section 5.2.

In the SLM process, the term $\dot{Q}$ in the energy conservation equation accounts for energy transfer between the fluid and its surroundings. This includes heat loss via convection, radiation, and evaporation, as well as laser energy input (e.g., absorbed energy P_a). The convective heat loss rate is

$$\dot{Q}_{\mathrm{con}} = h(T - T_0)$$

where h is the heat transfer coefficient, T is the fluid temperature, and T_0 is the environmental temperature (500 K in our simulations). The radiative heat loss rate is

$$\dot{Q}_{\mathrm{rad}} = \varepsilon\sigma(T^4 - T_0^4)$$

where ε is the emissivity and σ is the Stefan–Boltzmann constant. The evaporative heat loss rate is

$$\dot{Q}_{\mathrm{eva}} = jL_v$$

where j denotes the evaporation mass flux, given by

$$j = \frac{0.82M}{\sqrt{2\pi M R_g T}} p_0 \exp\left[\frac{L_v M}{R_g}\left(\frac{1}{T_v} - \frac{1}{T}\right)\right]$$

All heat loss terms are converted into equivalent volumetric terms following the similar approach used for the recoil pressure [19].

2.5. The cellular automaton (CA) model

The CA model was developed to simulate microstructure evolution during solidification in the SLM process through steps of nucleation, growth, capture, and remelting. The computational domain is discretized into uniform cubic cells, with the decentered square algorithm employed to reduce mesh-induced directional bias in preferential growth orientations [29,30]. Cells are classified as solid, liquid, or interface, where interface cells represent solid cells adjacent to at least one liquid cell.

Nucleation may occur within the liquid cells under undercooling conditions, with the nucleation probability of each liquid cell given by $n_{\mathrm{nuc}}V_{\mathrm{CA}}$, where V_{CA} is the cell volume and n_{nuc} is the nucleation density. This density is modeled using a Gaussian distribution as

$$n_{\mathrm{nuc}} = \frac{n_{\max}}{\Delta T_\sigma\sqrt{2\pi}} \int_0^{\Delta T} \exp\left[\frac{1}{2}\left(\frac{\Delta T - \Delta T_N}{\Delta T_\sigma}\right)^2\right] \mathrm{d}T$$

where $n_{\max}$ is the maximum nucleation density, ΔT is the undercooling (obtained from CFD results), ΔT_σ is the standard deviation of undercooling, and ΔT_N is the mean nucleation undercooling. The parameter ΔT_N refers to the average temperature difference below the equilibrium melting point at which nucleation occurs, representing the typical level of undercooling required for the initial formation of crystals within the liquid phase under the given conditions.

Upon nucleation, the liquid cells transition to interface cells with assigned random crystallographic orientations. The interface cells grow first, potentially capturing adjacent liquid cells as progeny. These captured cells subsequently inherit the orientation and transition to interface cells.

The growth velocity v_c of the interface cells depends on undercooling and is assumed to follow a polynomial law $v_c = a_c(\Delta T)^{n_c}$, where a_c and n_c are fitting parameters. An interface cell transforms into a solid cell once no liquid neighbors remain. The time step for the CA model is dynamically determined based on the maximum growth velocity $v_{c,\max}$ of all interface cells [31]

$$\Delta t_{\mathrm{CA}} = \beta \frac{\Delta x_{\mathrm{CA}}}{v_{c,\max}}$$

where Δx_{CA} is the cell size and β is a stabilization factor (set to 0.3). Remelting occurs if the temperature of a solid or interface cell exceeds the liquidus temperature, transitioning the cell back to a liquid state.

3. Experiments

Cube samples of 316L stainless steel were fabricated using the SLM® Solution 125HL system, with pore defects and their effects on the microstructure investigated. The fiber laser, operating at a wavelength of 1060 nm, features a beam spot diameter of 70 μm to 100 μm. The 316L stainless steel powder has a particle size range of 20 μm to 100 μm. Key process parameters include a laser beam power of 200 W, a scanning speed of 0.8 m/s, a hatch distance of 120 μm, and a powder layer thickness of 30 μm. The substrate was preheated to 200 °C, and a bidirectional scanning strategy (zigzag scan) was employed. The SLM was performed under an argon atmosphere with strict oxygen control, maintaining oxygen content below 0.05 wt.%.

Post-manufacturing, the samples were precisely sectioned along the building direction via electrical discharge machining. The cut surfaces were then mechanically polished and electropolished to achieve a high-quality finish. Microstructural analysis around the pore defects on the cut surfaces is conducted using electron backscatter diffraction (EBSD).

4. Simulations and material parameters

In our simulations, the powder layer thickness is approximately 80 μm. The environment temperature is set at $T_0 = 500$ K. Prior to scanning, the powder bed is preheated to 500 K, and the ambient pressure is maintained at $p_0 = 1.01 \times 10^5$ Pa. The laser beam radius is $r_b = 27.5$ μm. The computational mesh resolution is about 4 μm × 4 μm × 4 μm. In all CFD simulations, the scanning direction is along the positive x-direction. Material properties for the 316L stainless steel are listed in Table 1.

The CA model uses a mesh size of 1 μm × 1 μm × 1 μm. At each time step, the temperature field is interpolated from the CFD results. Key parameters are set as $a_c = 7.325 \times 10^{-6}$, $n_c = 3.12$, the maximum nucleation density $n_{\max} = 10^{15}$ m^{-3}, the standard deviation of undercooling $\Delta T_\sigma = 1$ K, and the mean nucleation undercooling $\Delta T_N = 25$ K [16,32]. Two main physical mechanisms of solidification in the SLM are considered: the epitaxial growth of substrate grains at the melt pool boundary and the nucleation of new grains in the liquid. A relatively

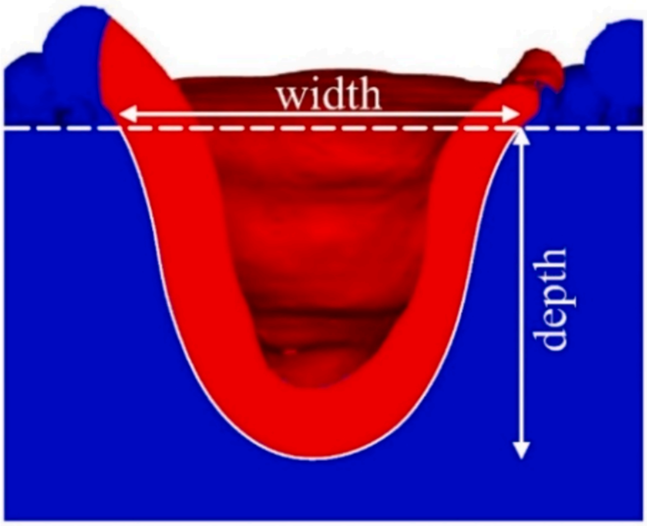

Fig. 6. Cross-sectional view of the melt pool from the CFD simulations. The dashed line represents the top surface of the initial substrate, while the red region indicates the melt pool.

Table 2
Comparison between our simulations and experimental results from ref. [33].

Scanning speed v_s (m/s)	Laser power P_l (W)	Depth (μm) (simulated/ experimental)	Width (μm) (simulated/ experimental)
1.2	200	73/68	98/104
1.8	300	72/65	103/94
1.5	200	57/57	96/84
1.5	400	127/119	110/103

high threshold value for ΔT_N is used, reflecting the rare occurrence of nucleation in the 316L stainless steel during SLM, as confirmed by our experiments and prior studies [32].

Simulation validation was performed by comparing melt pool geometry predictions (Fig. 6) with experimental data from ref. [33] under various scanning speeds and laser powers (Table 2). To match the experimental conditions, the powder size and layer thickness were adjusted to ensure a layer thickness of 30 μm, as in the experiments. The results show a strong agreement between simulations and experimental data (Table 2).

5. Melt pool in keyhole mode

Two distinct melt pool behaviors are commonly observed in the SLM process: keyhole mode and conduction mode, as demonstrated in Fig. 7. These modes are primarily distinguished by the interaction of the laser beam with the material and the resulting melt pool geometry [10,34]. In general, the melt pool in keyhole mode exhibits a depth-to-width ratio greater than 1, whereas in conduction mode, the ratio is typically less than 0.5.

The keyhole mode occurs when the ratio of the laser power density to scanning speed (q/v_s) is high enough to induce significant vaporization of the metal, forming a deep and narrow cavity within the melt pool, known as a keyhole (Fig. 7a). This keyhole geometry traps laser energy through multiple reflections, significantly enhancing energy absorption. However, the process can become unstable, with fluctuations in melt pool shape potentially leading to defects such as pores.

In contrast, the conduction mode occurs at relatively low ratio of q to v_s, resulting in a shallower, wider melt pool with a more uniform temperature distribution (Fig. 7b). Unlike keyhole mode, conduction mode lacks multiple reflections and significant vaporization, leading to more stable melt pool shapes and lower energy absorption. This reduced energy absorption and shallower melt pool increase the risk of incomplete melting of powder particles or weak inter-layer bonding, particularly in thick or multi-layered parts. These issues can undermine the mechanical performance of the final component.

Performing single-track scanning simulations, in section 5 we focus on the behavior of keyhole (Fig. 7a), with particular attention to the mechanisms of keyhole collapse. In section 6, we explore the mechanisms driving the conduction mode (Fig. 7b).

5.1. Mechanisms of keyhole collapse: Truncation and backfilling

During the SLM process, the keyhole continuously forms and collapses at the leading edge of the melt pool. As the surrounding molten metal rapidly fills the collapsing cavity, gas bubbles may become trapped within the solidifying material, leading to porosity. Such defects compromise the mechanical properties and overall quality of the final part, making keyhole collapse a critical issue in additive manufacturing that requires thorough investigation.

Truncation and backfilling are two key phenomena associated with

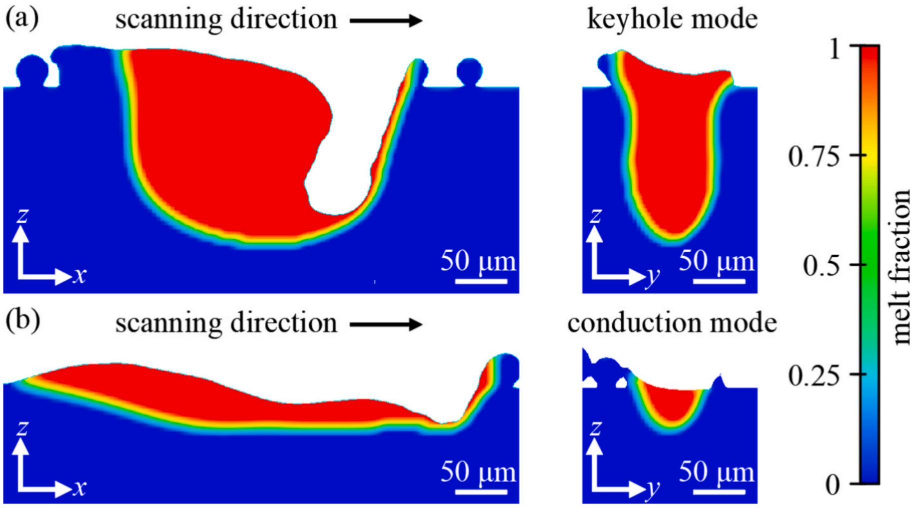

Fig. 7. Representative melt pool shapes in (a) keyhole mode ($P_l = 150$ W and $v_s = 0.5$ m/s) and (b) conduction mode ($P_l = 100$ W and $v_s = 1.2$ m/s). The melt fraction scale ranges from 0 (fully solid material) to 1 (fully molten material), with intermediate values representing a mixture of solid and liquid phases. Red regions here highlight the melt pool, with width along the y-axis and depth along the z-axis.

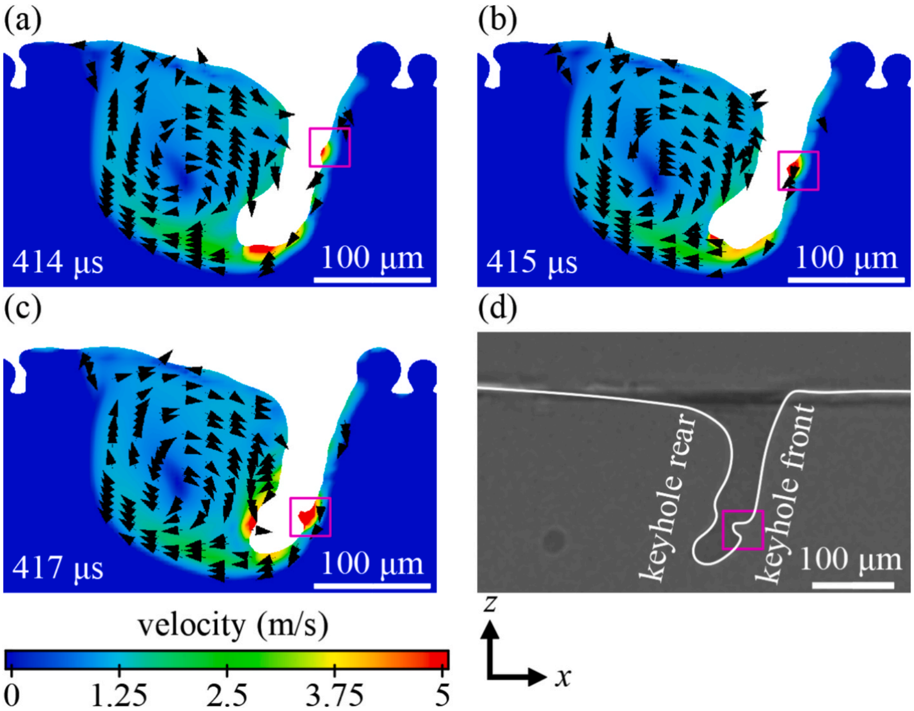

Fig. 8. (a-c) Velocity distribution of the molten metal in the melt pool in the center plane of the scanning track ($y = 0$). The laser power is $P_l = 150$ W, and the scanning speed is $v_s = 0.5$ m/s. A front protrusion on the keyhole surface could be observed. Scaled velocity vectors (black arrows with nearly uniform magnitudes) depict the flow patterns of molten metal within the melt pool. (d) Experimental observation of a front protrusion on the keyhole front wall, highlighted with a pink square [35].

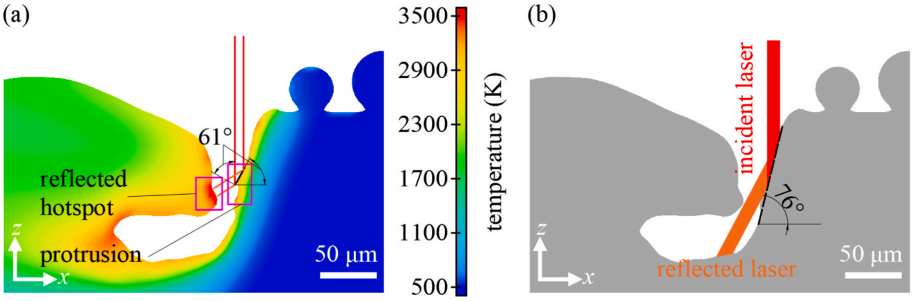

Fig. 9. Temperature distribution and laser reflection path in the melt pool at $y = 0$, highlighting the effect of the front protrusion on laser reflection. (a) Reflected laser rays bouncing off the front protrusion create a high-temperature spot on the rear wall of the keyhole, promoting protrusion development (CFD simulation at $t = 709.5$ μs). (b) Rough estimation of ray reflection using an average slope angle, showing that reflected rays in this case primarily strike the keyhole bottom rather than the rear wall.

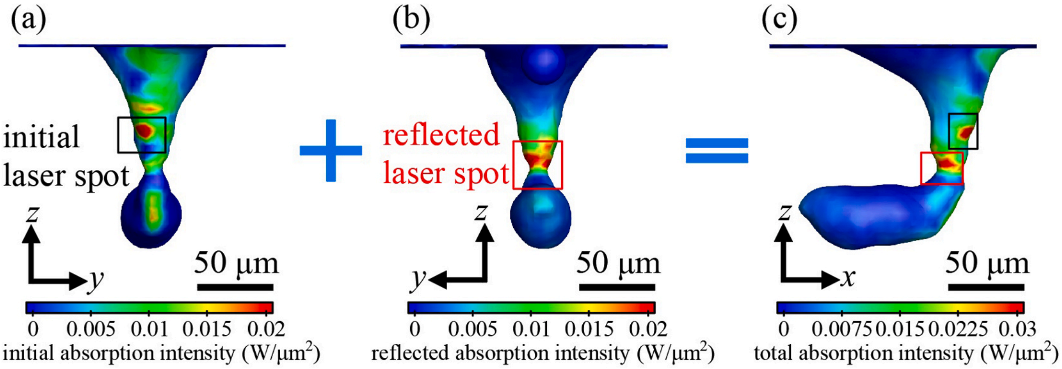

Fig. 10. Laser absorption intensity distribution on the keyhole surface for $P_l = 150$ W and $v_s = 0.5$ m/s at $t = 709.5$ μs. Panels show the intensity distributions for the initial laser ray absorption (a), reflected ray absorption (b), and combined absorption (c). The scanning direction is along the positive x-direction. The initial laser absorption marked in (a) is obstructed in (b), preventing it from being marked in (b).

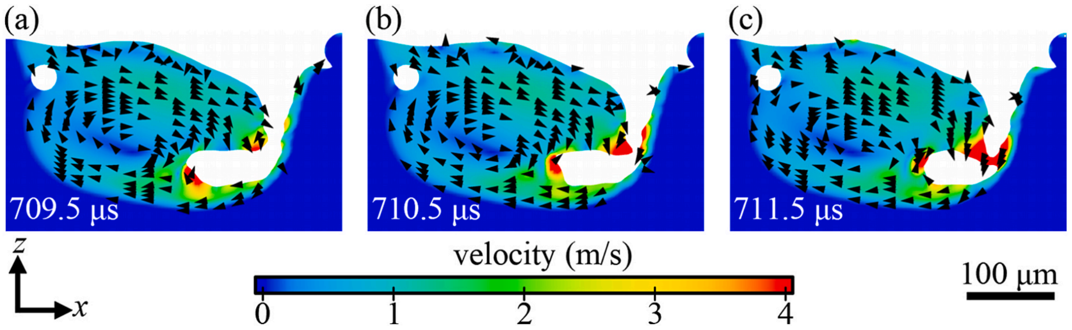

Fig. 11. Time sequence of numerical simulations in the center plane ($y = 0$) showing protrusion growth and merging, leading to the keyhole truncation ($P_l = 150$ W and $v_s = 0.5$ m/s). Black arrows represent scaled velocity vectors of the molten metal.

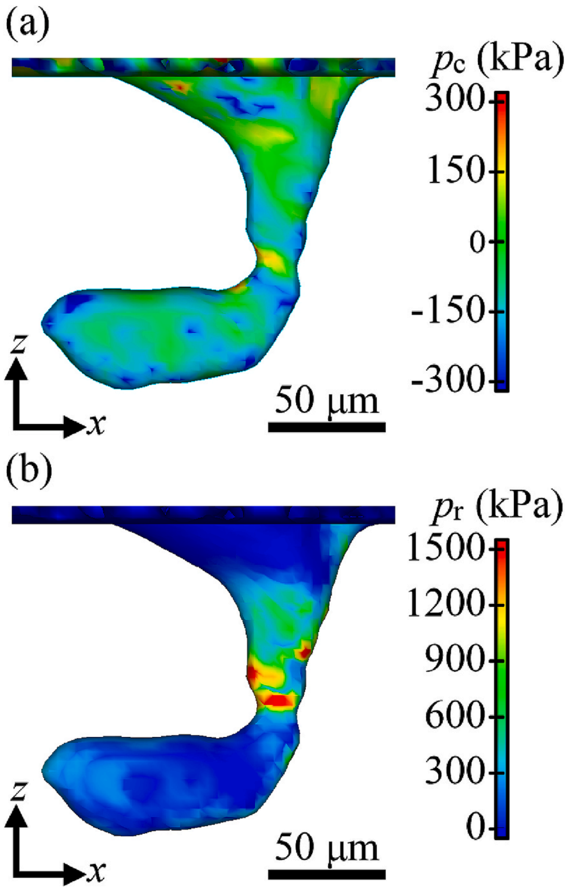

Fig. 12. Distributions of the capillary pressure p_c (a) and recoil pressure p_r (b) at the moment before keyhole closure ($t = 709.5$ μs) at $P_l = 150$ W and $v_s = 0.5$ m/s.

the behavior of the keyhole collapse in SLM.

Briefly speaking, truncation occurs when the keyhole is abruptly severed by the molten metal from the middle of the keyhole. The laser beam drives the molten metal to abruptly truncate the cavity, blocking gas and trapping a bubble in the melt pool. As the laser moves away, the melt pool solidifies around the bubble, leaving a pore defect in the material.

Backfilling, on the other hand, involves the collapse of the keyhole as molten metal flows back into the cavity. This typically occurs when the laser fails to maintain sufficient recoil pressure at the keyhole's base, allowing surface tension to dominate. The molten metal gradually fills the keyhole from the bottom up. If the laser reheats the metal, it can reestablish recoil pressure and prevent further backfilling. Unlike truncation, backfilling often displaces gas rather than trapping it, avoiding bubble formation.

Here, sections 5.1.1 and 5.1.2 delve into the morphological evolution of the keyhole during truncation and backfilling, analyzing the governing mechanisms. Particular attention is given to the influence of reflected laser rays on the rear wall of the keyhole, a factor often overlooked in previous studies.

5.1.1. Keyhole truncation: Protrusions and their merging

The keyhole truncation process unfolds in distinct stages, beginning with the formation of a molten metal protrusion at the leading edge of the keyhole. This protrusion alters the laser reflections and generates recoil pressure on the rear wall, which, in turn, induces a corresponding protrusion there. As these protrusions grow, they eventually merge, truncating the keyhole and trapping gas within the melt pool.

Using the CFD simulations, we examine the evolution of protrusions and their effects on laser-ray interactions with the keyhole surface, along with the distribution of recoil pressure. The simulations were performed at a laser power $P_l = 150$ W and a scanning speed $v_s = 0.5$ m/s (Figs. 8-12).

Fig. 8a-c shows the velocity distribution of the molten metal, highlighting a high-velocity protrusion on the front wall of the keyhole. The laser beam heats the upper surface of the front protrusion, generating localized recoil pressure that drives the protrusion downward. The molten metal at the protrusion attains velocities exceeding 5 m/s (Fig. 8b and c), significantly outpacing the surrounding fluid. As the protruding bulge descends, it assimilates surrounding molten metal, grows, and absorbs additional laser energy. Consequently, the protrusion near the keyhole base becomes notably larger than those above. The simulated front protrusion shows strong alignment with experimental observation [35].

As demonstrated by the flow pattern within the melt pool, recoil pressure drives the molten metal at the front wall of the keyhole upward from the keyhole bottom and toward the pool's rear, where it rises to the middle of the melt pool before recirculating forward, forming a primary clockwise flow, occupying most of the melt pool volume.

The bulging protrusion on the keyhole front wall significantly affects the energy absorption and laser reflection, driving the growth of the front protrusion and initiating a rear-wall protrusion (Fig. 9). In Fig. 9a, the small front protrusion has a slope angle of approximately 61°. When the laser interacts with this protrusion, the locally inclined reflecting surface increases the absorbed energy per unit area. Introducing η_s as the ratio of absorbed energy per unit area to the incident energy density, η_s is given by

$$\eta_s = (1 - R_{\text{eff}})\cos\theta_i,$$

where θ_i is the incidence angle, and R_{eff} is the effective reflectivity in Eq. (1). In Fig. 9a, we have $\theta_i = 61°$ and $\eta_s = 0.181$.

In contrast, if the small protrusion is absent on the keyhole surface and an average slope angle of the keyhole front wall is taken as the

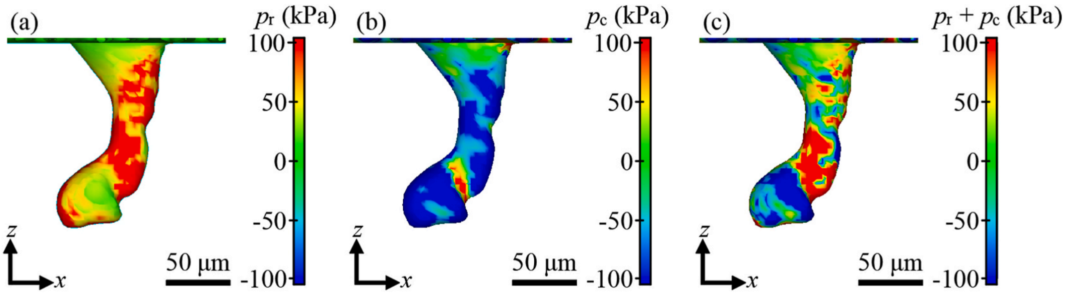

Fig. 13. Distribution of the recoil pressure p_r (a), capillary pressure p_c (b), and their summation $p_r + p_c$ (c) when the keyhole is about to backfill.

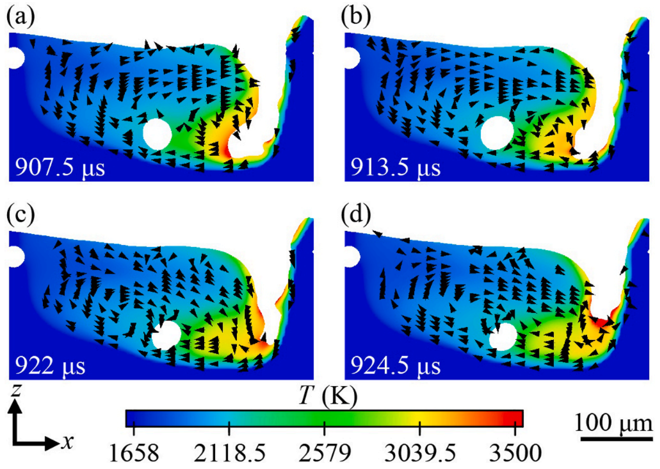

Fig. 14. The keyhole backfilling process at $y = 0$.

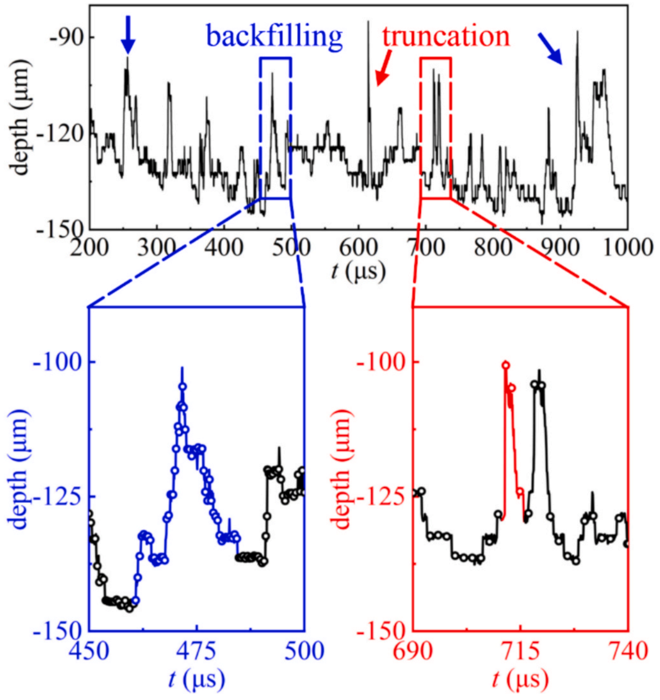

Fig. 15. Keyhole depth profiles versus time t at $P_l = 150$ W and $v_s = 0.5$ m/s. The red curve and arrows indicate truncation events, and the blue curve and arrows indicate backfilling events.

incidence angle, θ_i becomes 76° and $\eta_s = 0.1$ (Fig. 9b). This value of η_s can be regarded as a rough estimate over the keyhole front surface.

Comparing the values of η_s in Fig. 9a and b, one can see that the presence of the small front protrusion leads to a higher η_s, significantly enhancing the recoil pressure, which depends strongly on the local temperature proportional to η_s. The resulting increase in recoil pressure drives the rapid growth and downward movement of the front protrusion.

Moreover, laser rays reflected off the protrusion on the keyhole front wall strike the rear wall, creating a high-temperature spot. This spot generates recoil pressure, triggering the formation and downward propagation of a rear-wall protrusion. Together, the protrusions on the front and rear walls of the keyhole form a complementary pair.

To further elucidate the role of reflected laser rays in rear protrusion formation, mapping the laser absorption intensity offers a clearer perspective compared to analyzing only the temperature field and energy ratios (Fig. 10). Here, the laser absorption intensity (W/μm^2) is defined as the total power absorbed by a surface cell, divided by its area. This intensity is decomposed into contributions from direct incident rays and reflected rays.

Fig. 10 shows the absorption intensity on the keyhole surface at $t =$ 709.5 μs. High-intensity hotspots are observed on both the front and rear walls of the keyhole. The initial laser spot of interest is outlined with a black frame, while the corresponding reflected laser spot is marked with a red frame. These two spots correspond to protrusions that form a complementary pair. The hotspots on the keyhole front wall (Fig. 10a) are primarily due to direct laser absorption, concentrated on upper surfaces of the front protrusions, with a peak intensity exceeding 0.025 W/μm^2. Regions beneath the protrusions, shielded from the laser, exhibit minimal absorption (blue regions). Surrounding regions with inclined surfaces and larger incidence angles θ_i show reduced absorption, as indicated by green regions.

On the rear wall (Fig. 10b), absorption is dominated by reflected rays bouncing off the front protrusion (in the black frame), with peak intensity around 0.025 W/μm^2, sufficient to drive protrusion formation. In contrast, the sidewall absorption is lower due to weaker reflected rays, underscoring the critical role of reflections in energy distribution.

A previous study, unlike to our analysis, suggested that while the reflected laser significantly influences rear wall fluctuations, the distribution of the reflected laser rays is essentially random [36]. Consequently, the hot spots on the keyhole rear wall were proposed to occur randomly, whereas we observe that these spots typically form directly opposite the protrusion on the front wall (Fig. 10c). This discrepancy may arise from the larger laser radius used in their study. The increased radius enlarges the keyhole, thereby extending the propagation distance of the reflected laser beam. Due to the varying reflection angles at different positions on the keyhole front wall, the extended propagation distance causes the reflected laser's landing points to become more dispersed, making regularity difficult to discern.

Fig. 11 shows the process by which the protrusions grow, merge, and ultimately truncate the keyhole. The front and rear protrusions form a pair, driven downward by recoil pressure. As these protrusions approach

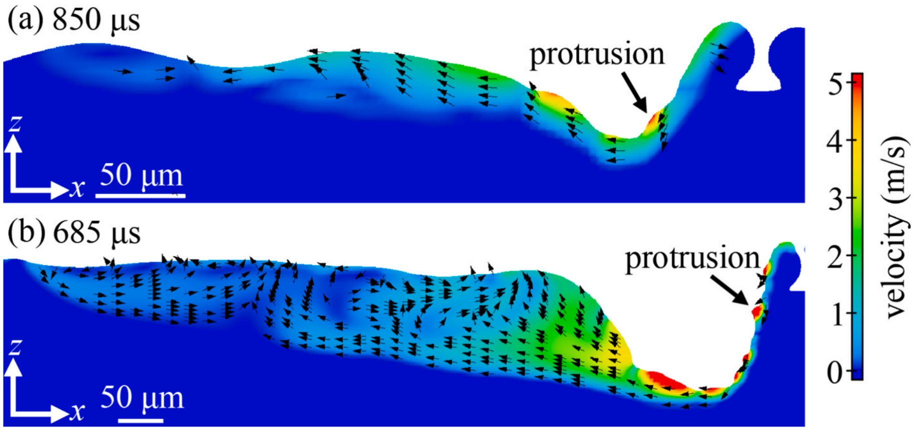

Fig. 16. Velocity distributions at $y = 0$ for the melt pool at (a) $P_l = 100$ W and $v_s = 1.2$ m/s, and (b) $P_l = 300$ W and $v_s = 1.2$ m/s. Panel (a) shows the melt pool in the conduction mode, while panel (b) depicts the transition between conduction and keyhole modes.

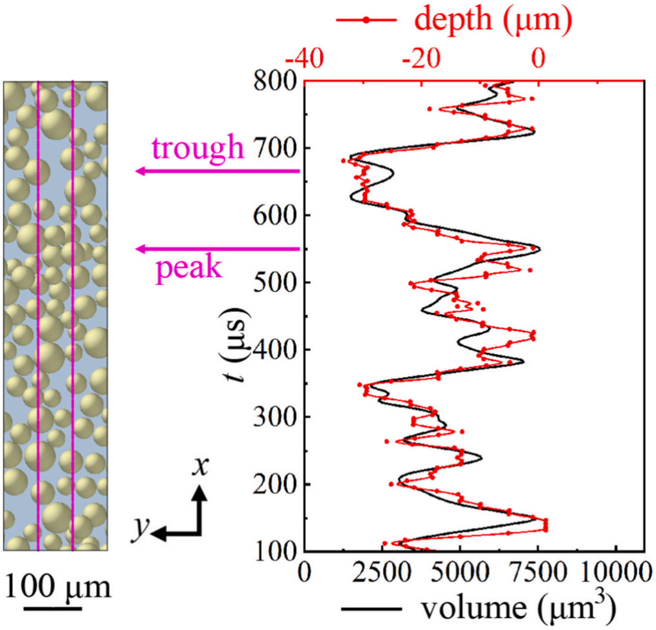

Fig. 17. The volume profile (black curve) of the initial powder particles within the melt track before scanning and the melt pool depth profile (red curve) during the scanning process at $P_l = 100$ W and $v_s = 1.2$ m/s. A strong correlation is observed between the particle volume profile and the melt pool depth profile. The melt track is approximately outlined by the pink lines in the powder bed panel (left).

each other (Fig. 11b at $t = 710.5$ μs), multiple laser reflections intensify the recoil pressure, promoting further protrusion growth. At $t = 711.5$ μs, the protrusions merge, truncating the keyhole and forming a gas bubble.

After truncation, a thin molten metal layer remains above the bubble, exposed to the laser. Due to the poor thermal conductivity of the gas bubble, the temperature in this layer rises rapidly, generating intense recoil pressure. This pressure may push the bubble downward or puncture the molten metal layer, reopening the bubble. If the bubble survives the recoil pressure and remains within the melt pool, it may be trapped in the solidifying metal as the pool cools, eventually forming a pore defect.

However, it is important to note that while truncation events are observed in nearly every simulation, not all lead to pore retention. In many instances, the bubbles do not survive. As a result, the likelihood of stable pore formation remains relatively low in the simulations. This observation is consistent with experimental outcomes, where 316L stainless steel demonstrates favorable forming quality with minimal porosity when appropriate scanning parameters are applied [33].

Distributions of the recoil pressure p_r in Eq. (2), capillary pressure p_c in Eq. (3), and Marangoni force in Eq. (4) on the keyhole surface are estimated to assess their roles in keyhole evolution. Under laser beam irradiation, the keyhole surface temperature rises rapidly, exceeding 4000 K in the hotspot region. As shown in Fig. 12b, the recoil pressure p_r on the keyhole wall reaches over 1500 kPa. For the surface tension, the magnitude of the keyhole curvature ranges between 10^4 m^{-1} and 10^5 m^{-1}, resulting in p_c estimated to be on the order of 10 kPa to 100 kPa. Fig. 12a further indicates that p_c on most keyhole wall regions remains below 300 kPa—nearly an order of magnitude lower than p_r. The Marangoni shear stress ($\sim(\mathrm{d}\gamma/\mathrm{d}T)[\nabla T - (\mathbf{n}\cdot\nabla T)\mathbf{n}]$), influenced by the tangential temperature gradient (on the order of 10^7 K/m) and surface tension coefficient ($-\mathrm{d}\gamma/\mathrm{d}T = 4.3 \times 10^{-4}$ N m^{-1} K^{-1}, Table 1), is on the order of 1 kPa—an order of magnitude smaller than the capillary pressure. In summary, the recoil pressure predominantly governs keyhole truncation, with the surface tension playing a secondary role. The Marangoni force and other factors (such as gravity at the micrometer scale) have insignificant effects on keyhole evolution and collapse.

5.1.2. Keyhole backfilling

In addition to truncation, backfilling is another key mechanism of keyhole collapse. During keyhole evolution, reflected laser rays heat the rear wall at the bottom of the keyhole, generating recoil pressure that pushes the molten metal backwards. Simultaneously, the descending molten metal from the front wall is obstructed by the solid–liquid interface at the bottom of the melt pool, forcing it to flow backwards as well. These combined effects cause the lower part of the keyhole to bend backwards into a J-shape rather than descending vertically.

Fig. 13 shows that the bottom section of the keyhole in the backfilling mode gradually curves backward, making it difficult for reflected laser rays to sufficiently heat the rear wall. As the recoil pressure diminishes, surface tension becomes dominant. With cooling at the rear wall, negative pressure develops, driving the liquid metal to fill the keyhole. Unlike truncation, backfilling typically does not lead to pore formation since the process begins at the bottom of the keyhole and progresses upward, allowing gas to escape through the open top.

Fig. 14 depicts the backfilling process. Initially, the curved portion of the J-shaped keyhole closes, restoring the keyhole to a near-vertical shape. The liquid metal then continues to flow upward, filling the middle of the keyhole. Once backfilling is complete, the keyhole is redrilled to its original depth and reverts to a J-shape under the laser's influence. Although no pore defects form during backfilling, the significant fluctuations in the keyhole depth may weaken bonding between

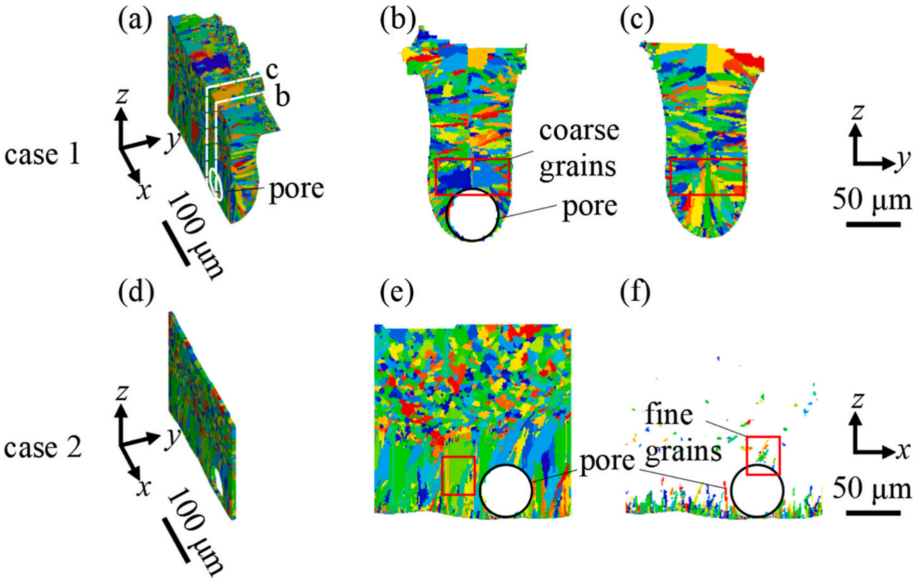

Fig. 18. (a) Material microstructure after single-track scanning, highlighting pore within white circle. Colors indicate different grains. White dashed lines b and c mark the cross-section locations for (b) with pore and (c) without a pore, respectively. Grains near pore in the red box in (b) are coarser than those in the red box in (c). A longitudinal slice (d) along pore is observed from the y-direction in (e). The panel (f) shows the same slice as (e) but excludes grains larger than 100 µm^3. Fine grains in the red box in (f) are smaller than neighboring grains in the red box in (e). Black circles in (b), (e), and (f) outline pore boundaries. Cases 1 and 2 refer to simulations performed incorporating stochastic variations in nucleation and growth processes, with the same parameters at $P_l = 150$ W and $v_s = 0.5$ m/s.

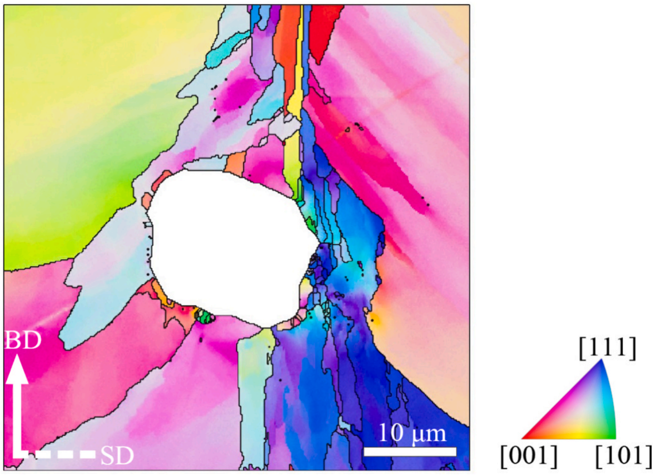

Fig. 19. EBSD image of the fine-grained region near the pore in experiments. The dashed line indicates the laser scanning direction (SD), along which the laser scanned bidirectionally. BD, building direction.

adjacent layers or tracks in the SLM. In the keyhole truncation process, both pore defects and interlayer bonding weaknesses, arising from keyhole depth fluctuations, are possible. Note that single-track simulations cannot fully capture defects that arise between layers or tracks.

5.2. *Keyhole evolution through truncation and backfilling*

Fig. 15 provides an overview of keyhole evolution by illustrating temporal variations in keyhole depth. Under stable conditions, the depth fluctuates within a narrow range, ensuring consistent bonding with the underlying material and preventing defect formation. However, intermittent collapse events—caused by truncation or backfilling—result in significant depth variations. During these events, the minimum depth can reach 85 µm, approximately 66 % of the average depth (129 µm), introducing instability that may lead to defects.

The magnified views in the red and blue boxes of Fig. 15 highlight the distinct depth variation profiles associated with truncation and backfilling. In the red box, the sharp rising edge signifies a sudden reduction in keyhole depth, characteristic of truncation, where the keyhole is severed at its middle part. One of the segments of the depth profile corresponding to truncation events is highlighted in red. Conversely, the blue curve shows a gentler rising edge and a longer duration, indicative of backfilling, where liquid gradually fills the keyhole from its bottom.

The differences in the temporal profiles of these collapse modes are evident in their durations. Backfilling peaks typically last longer due to the gradual nature of the filling process. As shown in Fig. 15, the backfilling peak duration is approximately 24 µs, over four times longer than the abrupt truncation mode.

6. Melt pool in conduction mode

We now analyze the dynamic behavior of the melt pool in conduction mode and the underlying physical mechanisms are analyzed here. In the conduction mode, the melt pool adopts a wide and shallow shape. As shown in Fig. 16a, small protrusions appear on the front wall, but they are significantly smaller than those observed in the keyhole mode, where protrusions from the keyhole's front wall can exceed 13 µm in height (Fig. 8). In the conduction mode, these protrusions are barely visible and can only be identified with the aid of velocity distribution data. They gradually move toward the rear of the melt pool, where they eventually dissipate. During the transition between the conduction and keyhole modes, the protrusions reach an intermediate height of approximately 8 µm (Fig. 16b).

The difference in protrusion behavior between the conduction and keyhole modes, as well as their transition, arises from the variation in energy absorption at the protrusions. In the conduction mode, the lower average slope angle of the front wall profile significantly reduces the incident angle θ_i, limiting the ability of protrusions to enhance localized energy absorption by altering the shape of the front wall, as illustrated in Fig. 9a. In the conduction mode, the laser beam exits the melt pool without undergoing multiple reflections, and the energy absorbed from the reflected rays is minimal. This is in stark contrast to the keyhole mode, where a substantial amount of energy is absorbed by the rear wall

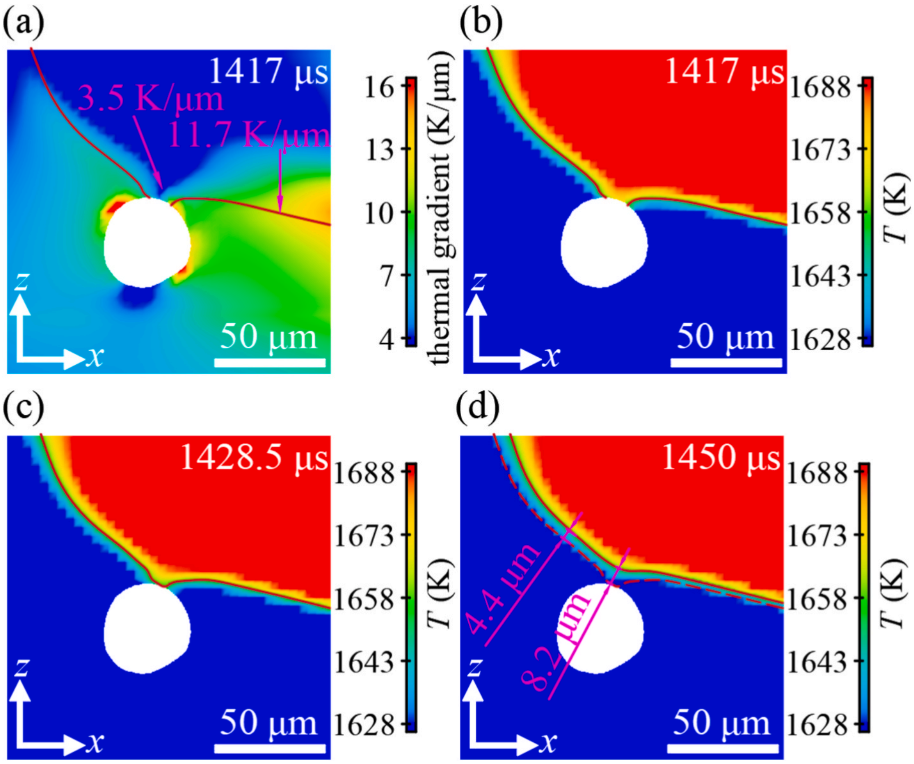

Fig. 20. Temperature field near pore in Fig. 18a. (a) A contour plot of the thermal gradient near pore at the CFD simulation time $t = 1417$ µs. (b-d) Temperature fields with the isotherm at the solidus temperature (1658 K, solid lines) at $t = 1417$ µs, 1428.5 µs, and 1450 µs, respectively. The dashed line in (d) marks the position of the solidus temperature isotherm from (c).

of the keyhole. Moreover, the wider separation between the front and rear walls of the melt pool in the conduction mode further mitigates the concentration of reflected laser beams on the rear wall, which can remain relatively smooth and free of downward-moving protrusions.

In addition to directly analyzing the melt pool, differences between the conduction and keyhole modes can be discerned from the characteristics of their depth fluctuations over time. Although the melt pool in the conduction mode exhibits fluctuations, their nature is distinctly different from those observed in the keyhole mode. As shown in Fig. 15, the keyhole mode is characterized by numerous sharp peaks with very short durations, primarily caused by truncation and backfilling events. In contrast, melt pool depth fluctuations in the conduction mode, indicated by the red line in Fig. 17, lack sharp peaks. Instead, they feature broader peaks and troughs with durations ranging from tens to over 100 µs, reflecting a stable melt pool without collapse events akin to those in the keyhole mode.

To further explore the depth fluctuations in the conduction mode, the volume profile of the initial powder particles in the melt track, prior to scanning, is compared with the depth profile of the melt pool in Fig. 17. A strong correlation is observed between these two profiles. Notably, the depth peaks and troughs (marked by pink arrows) correspond well with regions of dense and sparse powder particle distributions. These observations collectively suggest that the melt pool depth fluctuations in the conduction mode are significantly influenced by the nonuniform distribution of powder particles.

In the keyhole mode, however, the influence of nonuniform powder distribution appears minimal. In Fig. 15, the scanning speed (0.5 m/s) in the keyhole mode is slower than in the conduction mode (1.2 m/s) in Fig. 17, costing the laser beam more time to traverse the same distance on the powder bed. If nonuniform powder distribution had a significant influence in the keyhole mode, one would expect to observe depth fluctuation peaks with longer durations compared to those in the conduction mode. Since such peaks are absent in Fig. 15, we conclude that powder bed unevenness does not have a pronounced effect on the melt pool depth in the keyhole mode.

7. Microstructure surrounding pores

Stress concentration and crack nucleation usually occur around pore defects, significantly impacting mechanical properties of structural components. These effects are closely tied to the local microstructure. For instance, reductions in grain size have been shown to facilitate localized crack propagation and lower the threshold stress intensity [37,38]. By integrating CFD-derived thermal field data with a CA model, we simulate microstructure evolution during solidification in the SLM process, encompassing nucleation, growth, capture, and remelting, with a particular focus on the microstructure near pores and its underlying mechanisms.

Pores play a dual role in microstructure evolution by obstructing grain growth and reducing the local thermal gradient. The dual effects of pores on grain refinement and coarsening are demonstrated in Fig. 18, which shows two CA simulations with identical computational parameters but incorporating stochastic variations in nucleation and growth processes. As shown in Fig. 18b, the pore obstructs the progression of columnar grains, forcing them to deviate and bypass the pore. For instance, columnar grains below pore are blocked, allowing more space for grains near the pore's top to grow. In contrast, Fig. 18c indicates columnar grains advancing diagonally upward from the melt pool edges toward the center, where competitive growth occurs, suppressing adjacent grains. Consequently, grain sizes above the pore, highlighted in the red box of Fig. 18b, are larger than those in the pore-free region shown in Fig. 18c, aligning with prior simulations [39].

In our 316L stainless steel experiments, regions of finer grains adjacent to pores are also observed (Fig. 19). This phenomenon is attributed to the pore's influence on the thermal field. Acting as thermal insulators with low conductivity, pores impede heat dissipation, reducing the local thermal gradient and promoting the formation of fine grains.

To further elucidate the influence of pores on heat dissipation, we analyze the thermal field using the CFD simulations during the moment the solid–liquid interface traverses a pore. In Fig. 20a, the thermal gradient near the solidus isotherm (red line) above the pore is approximately 3.5 K/μm, compared to 11.7 K/μm away from the pore. This reduced gradient causes the isotherm to bend as it passes over the pore (Fig. 20c) before smoothing out again (Fig. 20d). In Fig. 20d, the dashed line marks the position of the solidus temperature isotherm from Fig. 20c. Between the dashed and solid red lines, representing solidification over 21.5 μs, the region above the pore spans 8.2 μm, compared to 4.4 μm in adjacent areas, indicating a higher local solidification rate. As a result, the reduced thermal gradient-to-solidification rate ratio near the pore promotes nucleation and fine-grain growth. In the red box of Fig. 18f, fine grains above the pore are smaller than nearby grains in Fig. 18e.

8. Conclusion

This study integrates ray-tracing heat source modeling with CFD simulations to explore melt pool evolution and pore defect formation mechanisms in the SLM process. A cellular automaton model is further used to assess the impact of pore defects on the surrounding microstructure. The key findings are summarized below.

(1) In the keyhole mode, where a deep and narrow vapor cavity forms in the melt pool due to the high-intensity laser beam, the recoil pressure generates protrusions on the keyhole's front wall, while reflected laser rays induce protrusions on the rear wall. Their mergence traps gas at the keyhole bottom, causing keyhole truncation—a primary collapse mechanism leading to pore defects in SLM.

(2) Backfilling represents another primary mode of keyhole collapse, occurring when keyhole curvature prevents the laser from reaching the bottom. This reduces local recoil pressure, allowing surface tension to drive liquid backfilling. By facilitating gas escape through the open top of the keyhole, backfilling typically does not lead to the formation of pore defects.

(3) In the conduction mode, protrusions are smaller and exert less influence on the melt pool compared to the keyhole mode. The nonuniform distribution of powder particles emerges as the primary cause of melt pool depth fluctuations in the conduction mode.

(4) Pores have competing effects on microstructure, influencing it by obstructing grain growth and altering the thermal field. While pore obstruction provides more space for grains near the pore's top to grow, the reduced thermal gradients around pores promote the formation of finer grains. These dual mechanisms—grain coarsening and fine-grain formation—affect the resulting mechanical properties.

CRediT authorship contribution statement

Jiafei Pang: Writing – original draft, Methodology, Investigation, Formal analysis. **Liming Huang:** Methodology, Investigation. **Hailin Liu:** Methodology, Investigation. **Xin Yi:** Writing – review & editing, Project administration, Methodology, Investigation, Funding acquisition, Conceptualization.

Declaration of competing interest

The authors declare that they have no known competing financial interests or personal relationships that could have appeared to influence the work reported in this paper.

Acknowledgments

This work was supported by the National Natural Science Foundation of China (grant no. 11988102). Computation resources supported by the High-performance Computing Platform of Peking University are acknowledged.

Data availability

Data will be made available on request.

References

[1] E.O. Olakanmi, R.F. Cochrane, K.W. Dalgarno, A review on selective laser sintering/melting (SLS/SLM) of aluminium alloy powders: Processing, microstructure, and properties, Prog. Mater. Sci. 74 (2015) 401–477.

[2] N.T. Aboulkhair, N.M. Everitt, I. Ashcroft, C. Tuck, Reducing porosity in AlSi10Mg parts processed by selective laser melting, Addit. Manuf. 1–4 (2014) 77–86.

[3] H. Gong, K. Rafi, H. Gu, G.J. Ram, T. Starr, B. Stucker, Influence of defects on mechanical properties of Ti–6Al–4V components produced by selective laser melting and electron beam melting, Mater. Des. 86 (2015) 545–554.

[4] S.A. Khairallah, A.T. Anderson, A. Rubenchik, W.E. King, Laser powder-bed fusion additive manufacturing: Physics of complex melt flow and formation mechanisms of pores, spatter, and denudation zones, Acta Mater. 108 (2016) 36–45.

[5] X. Ren, H. Liu, F. Lu, L. Huang, X. Yi, Effects of processing parameters on the densification, microstructure and mechanical properties of pure tungsten fabricated by optimized selective laser melting: From single and multiple scan tracks to bulk parts, Int. J. Refract. Met. Hard Mater. 96 (2021) 105490.

[6] F.-y. Lu, H.-y. Wan, X. Ren, L.-m. Huang, H.-l. Liu, X. Yi, Mechanical and microstructural characterization of additive manufactured Inconel 718 alloy by selective laser melting and laser metal deposition, J. Iron Steel Res. Int. 29 (2022) 1322–1333.

[7] L. Huang, H. Wan, Q. Han, J. Wang, X. Yi, Mitigating surface notches for enhanced fatigue performance of metallic gyroid structures via contour scanning, Int. J. Mech. Sci. 286 (2025) 109913.

[8] W. Yan, W. Ge, Y. Qian, S. Lin, B. Zhou, W.K. Liu, F. Lin, G.J. Wagner, Multi-physics modeling of single/multiple-track defect mechanisms in electron beam selective melting, Acta Mater. 134 (2017) 324–333.

[9] L. Du, W.-G. Jiang, G.-G. Xu, Q.-H. Qin, D.-S. Li, Finite element analysis and computational fluid dynamics verification of molten pool characteristics during selective laser melting of Ti-6Al-4V plates, 3D Print, Addit. Manuf. 10 (2023) 711–722.

[10] W.E. King, H.D. Barth, V.M. Castillo, G.F. Gallegos, J.W. Gibbs, D.E. Hahn, C. Kamath, A.M. Rubenchik, Observation of keyhole-mode laser melting in laser powder-bed fusion additive manufacturing, J. Mater. Process. Technol. 214 (2014) 2915–2925.

[11] T. DebRoy, H.L. Wei, J.S. Zuback, T. Mukherjee, J.W. Elmer, J.O. Milewski, A. M. Beese, A. Wilson-Heid, A. De, W. Zhang, Additive manufacturing of metallic components – process, structure and properties, Prog. Mater Sci. 92 (2018) 112–224.

[12] K.Q. Le, C. Tang, C.H. Wong, On the study of keyhole-mode melting in selective laser melting process, Int. J. Therm. Sci. 145 (2019) 105992.

[13] C. Qiu, C. Panwisawas, M. Ward, H.C. Basoalto, J.W. Brooks, M.M. Attallah, On the role of melt flow into the surface structure and porosity development during selective laser melting, Acta Mater. 96 (2015) 72–79.

[14] W.-G. Jiang, G.-G. Xu, Q. Li, Q.-H. Qin, M.-L. Li, Y.-Y. Sun, Improvement of wetting and necking of nickel-based superalloys fabricated by sequential dual-laser powder bed fusion via particle-scale computational fluid dynamics, Addit. Manuf. 59 (2022) 103203, https://doi.org/10.1016/j.addma.2022.103203.

[15] Y. Yang, P. Kühn, M. Yi, H. Egger, B.-X. Xu, Non-isothermal phase-field modeling of heat–melt–microstructure-coupled processes during powder bed fusion, JOM 72 (2020) 1719–1733.

[16] R. Shi, S.A. Khairallah, T.T. Roehling, T.W. Heo, J.T. McKeown, M.J. Matthews, Microstructural control in metal laser powder bed fusion additive manufacturing using laser beam shaping strategy, Acta Mater. 184 (2020) 284–305.

[17] P. Tan, R. Kiran, K. Zhou, Effects of sub-atmospheric pressure on keyhole dynamics and porosity in products fabricated by selective laser melting, J. Manuf. Process. 64 (2021) 816–827.

[18] J.L. Tan, C. Tang, C.H. Wong, A computational study on porosity evolution in parts produced by selective laser melting, Metall. Mater. Trans. A 49 (2018) 3663–3673.

[19] C. Tang, J.L. Tan, C.H. Wong, A numerical investigation on the physical mechanisms of single track defects in selective laser melting, Int. J. Heat Mass Tran. 126 (2018) 957–968.

[20] Z. Xiang, M. Yin, Z. Deng, X. Mei, G. Yin, Simulation of forming process of powder bed for additive manufacturing, J. Manuf. Sci. Eng. 138 (2016) 081002.

[21] D. Gueyffier, J. Li, A. Nadim, R. Scardovelli, S. Zaleski, Volume-of-fluid interface tracking with smoothed surface stress methods for three-dimensional flows, J. Comput. Phys. 152 (1999) 423–456.

[22] C.W. Hirt, B.D. Nichols, Volume of fluid (VOF) method for the dynamics of free boundaries, J. Comput. Phys. 39 (1981) 201–225.

[23] J. Ahn, S.-J. Na, Three-dimensional thermal simulation of nanosecond laser ablation for semitransparent material, Appl. Surf. Sci. 283 (2013) 115–127.

[24] T.I. Zohdi, Rapid simulation of laser processing of discrete particulate materials, Arch. Comput. Methods Eng. 20 (2013) 309–325.

[25] B. Liu, G. Fang, L. Lei, W. Liu, A new ray tracing heat source model for mesoscale CFD simulation of selective laser melting (SLM), Appl. Math. Model. 79 (2020) 506–520.

[26] H. Liu, J. Pang, J. Wang, X. Yi, New heat source model for accurate estimation of laser energy absorption near free surface in selective laser melting, Extreme Mech. Lett. 56 (2022) 101894.

[27] F. Rosler, D. Bruggemann, Shell-and-tube type latent heat thermal energy storage: numerical analysis and comparison with experiments, Heat Mass Transf. 47 (2011) 1027–1033.

[28] Z.S. Saldi, Marangoni Driven Free Surface Flows in Liquid Weld Pools, Delft University of Technology, The Netherlands, 2012. Ph.D. Thesis.

[29] C.A. Gandin, M. Rappaz, A coupled finite element-cellular automaton model for the prediction of dendritic grain structures in solidification processes, Acta Metall. Mater. 42 (1994) 2233–2246.

[30] C.A. Gandin, M. Rappaz, A 3D cellular automaton algorithm for the prediction of dendritic grain growth, Acta Mater. 45 (1997) 2187–2195.

[31] F. Xiong, Z. Gan, J. Chen, Y. Lian, Evaluate the effect of melt pool convection on grain structure of IN625 in laser melting process using experimentally validated process-structure modeling, J. Mater. Process. Technol. 303 (2022) 117538.

[32] A. Baumard, D. Ayrault, O. Fandeur, C. Bordreuil, F. Deschaux-Beaume, Numerical prediction of grain structure formation during laser powder bed fusion of 316L stainless steel, Mater. Des. 199 (2021) 109434.

[33] C. Kamath, B. El-dasher, G.F. Gallegos, W.E. King, A. Sisto, Density of additively-manufactured, 316L SS parts using laser powder-bed fusion at powers up to 400 W, Int. J. Adv. Manuf. Technol. 74 (2014) 65–78.

[34] N.T. Aboulkhair, I. Maskery, C. Tuck, I. Ashcroft, N.M. Everitt, On the formation of AlSi10Mg single tracks and layers in selective laser melting: Microstructure and nano-mechanical properties, J. Mater. Process. Technol. 230 (2016) 88–98.

[35] C. Zhao, Q. Guo, X. Li, N. Parab, K. Fezzaa, W. Tan, L. Chen, T. Sun, Bulk-explosion-induced metal spattering during laser processing, Phys. Rev. X 9 (2019) 021052.

[36] N. Kouraytem, X. Li, R. Cunningham, C. Zhao, N. Parab, T. Sun, A.D. Rollett, A. D. Spear, W. Tan, Effect of laser-matter interaction on molten pool flow and keyhole dynamics, Phys. Rev. Appl. 11 (2019) 064054.

[37] J.P. Sippel, E. Kerscher, Properties of the fine granular area and postulated models for its formation during very high cycle fatigue—A review, Appl. Sci. 10 (2020) 8475.

[38] J.P. Lucas, W.W. Gerberich, Low temperature and grain size effects on threshold and fatigue crack propagation in a high strength low alloy steel, Mater. Sci. Eng. 51 (1981) 203–212.

[39] R. Xu, W. Nan, Analysis of the metrics and mechanism of powder spreadability in powder-based additive manufacturing, Addit. Manuf. 71 (2023) 103596.